Journal of Materials Chemistry A

ROYAL SOCIETY OF CHEMISTRY

PAPER

View Article Online
View Journal | View Issue

Cite this: J. Mater. Chem. A, 2025, 13, 1172

A high power metal-supported protonic ceramic fuel cell using increased proton conductivity in the cathode functional layer of $La_{1-x}Sr_xScO_3$ (LSSc, x = 0.1–0.25)†

Hyo-Young Kim, [a] Motonori Watanabe,[ab] Jun Tae Song, [bc] Miki Inada[bc] and Tatsumi Ishihara *[abc]

Metal-supported protonic ceramic fuel cells (PCFCs) are highly attractive due to their high efficiency, reliability, and low cost. However, until now, there are limited reports on metal-supported PCFCs. In this study, a selective reduction method was used for preparing the metal-supported $BaZr_{0.44}Ce_{0.36}Y_{0.2}O_3$ (BZCY) cell. It was found that insertion of an $La_{1-x}Sr_xScO_3$ (LSSc, x = 0.1–0.25) cathode functional film (CFL) was highly effective for decreasing cathodic overvoltage and ohmic loss, leading to significant increase in power density. Among the examined compositions, $La_{0.85}Sr_{0.15}ScO_3$ was identified as the optimal composition of the CFL. With this configuration, an open circuit voltage (OCV) of 1.15 V and a maximum power density (MPD) of 233 mW cm^{-2} were achieved at 773 K. Impedance analysis suggests that the increased power density can be attributed to the decreased overvoltage and ohmic loss in the cathode side, due to significantly increased proton conductivity in the LSSc film. This improvement is likely the result of the high concentration of H^+ in the LSSc film, as indicated by thermogravimetric (TG) and Hall effect measurement. Another challenge in PCFCs is the leakage current at higher oxygen partial pressure. However, the LSSc CFL also effectively prevented H^+ crossover, resulting in the OCV being almost the same as the theoretical value. Achieving near-theoretical OCV is crucial for the high energy conversion efficiency of PCFCs.

Received 23rd September 2024
Accepted 22nd November 2024

DOI: 10.1039/d4ta06783e

rsc.li/materials-a

1. Introduction

Fuel cells are expected to be highly efficient power generators without producing air pollutants like NO_x. Among the several types of fuel cells, solid oxide fuel cells (SOFCs), which use oxide ion conductors, exhibit particularly high energy conversion efficiencies, higher than 60%.[1–3] However, the high operating temperature (973–1273 K) of SOFCs leads to rapid degradation and unwanted reactions between components. Therefore, decreasing the operating temperature has been a crucial requirement.[4,5] In comparison to the oxide ion, the ionic radius of protons (H^+) is small, and so high ion conductivity is achieved at an intermediate temperature around 773 K.[6] As a result, high power densities can be realized at these intermediate temperatures compared to SOFCs.[7,8] In proton-conducting solid oxide fuel cells (PCFCs), water is generated at the cathode side after the electrochemical oxidation of the fuel, which prevents fuel dilution.[9] This feature enhances fuel utilization and contributes to a high energy conversion efficiency (>75%). Despite these advantages, the performance of current PCFCs is limited by slow cathodic reaction kinetics.[10–12] Decreasing the interfacial resistance between the electrolyte and cathode is required for achieving high-performance PCFCs at intermediate

[a]Department of Automotive Science, Graduate School of Integrated Frontier Sciences, Kyushu University, 744 Motooka, Nishi-Ku, Fukuoka, 819-0395, Japan. E-mail: ishihara@cstf.kyushu-u.ac.jp

[b]International Institute for Carbon Neutral Energy Research (WPI-I^{2}CNER), Kyushu University, 744 Motooka, Nishi-Ku, Fukuoka, 819-0395, Japan

[c]Department of Applied Chemistry, Faculty of Engineering, Kyushu University, 744 Motooka, Nishi-Ku, Fukuoka, 819-0395, Japan

† Electronic supplementary information (ESI) available: *I–V* curve and temperature dependence of MPD and OCV of the cell using LSSc15 (Fig. S1), comparison of the maximum power density with different Sr dopants (Fig. S2), EIS spectra of cathodic non, LSSc10, LSSc20, and LSSc25 CFL at 973 K (Fig. S3), (a) SEM and (b) EDS-mapping image of the cross-section after the cell test (Fig. S4), (a) hole mobility, (b) carrier concentration, (c) conductivity of BZCY film under humidified (3% H_2O) H_2 conditions (Fig. S5), FT-IR spectra of LSSc and BZCY film after exposure to humidified conditions (Fig. S6). The internal resistance of dry and humidified O_2 using LSSc15 CFL (Fig. S7), comparison of OCV and MPD with conventional PCFCs and the proposed cell (LSSc CFL) (Fig. S8), schematic image of PCFC preparation (Fig. S9), elemental composition of LSSc20 bulk and film (Table S1), comparison of the anode support before and after the reaction (Table S2), the measured PCFCs with LSSc CFL in this study at 973 K (Table S3), comparison of conventional PCFCs with the BZCY electrolyte (Table S4). See DOI: https://doi.org/10.1039/d4ta06783e

temperatures. This study investigates the effects of a thin LSSc perovskite interlayer as a cathode functional layer (CFL) in PCFCs, with the focus on its enhanced proton conductivity.[13,14] La-based perovskites are known to have high ionic conductivity and lattice deficiencies induced by A-site dopants with a large ionic radius. It enhances proton mobility and expands the conduction path.[15–17] Furthermore, Farlenkov *et al.* reported the excellent chemical stability of LSSc,[18] which is effective for increasing the overall stability of the cell. However, $LaScO_3$-based proton conductors as CFLs have not been studied, mainly due to the significant volume changes caused by hydration. This study examines the effects of a thin LSSc film as a CFL for stable operation and enhanced PCFC performance. To optimize gas diffusion and achieve high power density at intermediate temperatures, thin LSSc films were deposited using pulsed laser deposition (PLD). PLD is a promising deposition technique due to its advantages such as high deposition rate, uniform film, thickness control, and the ability to achieve desirable stoichiometry.[19–23] Employing thin LSSc films as a CFL on a BZCY/porous Ni–Fe bimetallic support is expected to decrease interfacial resistance and enhance cathodic performance due to the high hydration property of LSSc. It is also important to note that metal supported SOFCs are essential for the reliability of fuel cells. However, research on metal-supported PCFCs is still limited, and an important subject in terms of reliability as power generators.

2. Results and discussion

Fig. 1 shows the XRD patterns of LSSc bulk and film prepared by the PLD method. The XRD pattern of the LSSc bulk sample well agreed with the single-phase $LaScO_3$ structure (JSPDS no. 24-0562). In Fig. 1a, the XRD peaks of the LSSc bulk sample were shifted to a higher angle, suggesting that the partial substitution of Sr into the La-site was successfully achieved. Although the ionic radius of Sr^{2+} with coordination number 12 is slightly larger (14.4 pm) than that of La^{3+} (13.6 pm),[24] substitution of Sr^{2+} forms oxygen vacancies from the charge neutrality and these vacancies decrease the *d*-spacing within the lattice, since Sivakumar and Lesnichyova *et al.* reported that Sr doping in perovskites such as $LaFeO_3$ and $LaScO_3$ results in the formation of oxygen vacancies which caused lattice shrinkage and shifted the XRD pattern to a higher angle.[25,26] Fig. 1b shows the XRD patterns of the LSSc film, which consist of strong diffraction peaks, indicating a preferred orientation of growth direction, roughly the (010) orientation. Except for this, no diffraction peaks from impurity phases were observed, and so a single-phase LSSc film with orientation was deposited. In the case of the LSSc film, specific diffraction peaks from the (020), (040), and (161) planes were strengthened compared to those of the bulk sample, suggesting a preferred orientation of *b* lattice direction. The elemental composition of the LSSc film was analysed using XRF, and the composition was estimated to be 36.32, 8.34, and 55.33 at% of La, Sr, and Sc, respectively as shown in Table S1.† It seems that the composition of the film is close to that of the LSSc bulk sample. These results suggest that the partially oriented LSSc film of $La_{0.8}Sr_{0.2}ScO_3$ (LSSc20) was successfully deposited by PLD under 0.67 Pa and 180 mJ per pulse at 1073 K.

For the deposition of a uniform and dense electrolyte film, an NiO–$NiFe_2O_4$ precursor substrate with a dense and smooth surface is essential. After reduction of the NiO–$NiFe_2O_4$ substrate at 973 K, a porous Ni–Fe bimetallic substrate was obtained without significant volume change, as shown in Table S2.† Using this NiO–$NiFe_2O_4$ substrate, the effects of the LSSc CFL on the power generation properties of the BZCY/Ni–Fe porous support were studied.

Fig. 2 shows the power generation profiles of single PCFCs using humidified O_2 and H_2 as the oxidant and fuel, respectively. After reduction at 973 K for 1 h, PCFCs with and without LSSc CFL show a stable OCV around 0.95 V. This indicates that no cracks or pinholes formed during the reduction process and the oxygen pressure difference between the anode and cathode was maintained, confirming the absence of mechanical leakage after reduction. In comparison to the non CFL cell, the OCV of which was 0.95 V, the LSSc CFL exhibited a higher OCV of 1.04 V at 973 K, as shown in Fig. 2a. This higher OCV may result from the lower hole conduction of the LSSc CFL compared to the BZCY electrolyte under high pO_2 conditions. Among the LSSc compositions, the LSSc15 CFL shows the highest OCV and the largest maximum power density of 668 mW cm^{-2} at 973 K (non-CFL, LSSc10, LSSc20, and LSSc25 CFLs showed 139, 460, 521, and 353 mW cm^{-2}, respectively). At 773 K, an increase in OCV was observed due to the increased proton transport number (Fig. 2b). OCVs of PCFCs with non CFL, LSSc10, LSSc 15, LSSc20, and LSSc25 CFLs were 1.03, 1.09, 1.15, 1.11 and 1.10 V, respectively, at 773 K, which were almost the same as the theoretical OCV (1.15 V) calculated using the Nernst equation, compared to other proton conductors used as CFLs. This suggests that leakage current was suppressed by the LSSc CFL.

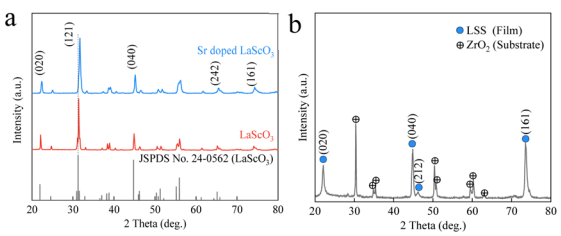

Fig. 1 XRD pattern of (a) LSc, LSSc bulk, and (b) LSSc film on a ZrO_2 substrate.

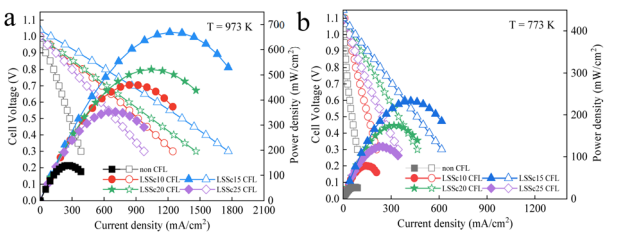

Fig. 2 *I*–*V* and *I*–*P* curve of PCFCs with non, LSSc10, LSSc15, LSSc20, and LSSc25 CFL at (a) 973 and (b) 773 K.

Fig. S1† shows the power generation property of the cell with the LSSc15 CFL as a function of temperature. The power densities of the cell using the LSSc15 CFL were 668, 405, and 233 mW cm^{-2} at 973, 873, and 773 K, respectively. The higher ionic conductivity of BZCY and the increased electrochemical activity of the electrode due to the presence of CFL resulted in a higher power density in the intermediate temperature range. Fig. S2† also shows that the 15% Sr doped $LaScO_3$ (LSSc15) shows the highest performance. At 773 K, the effects of the LSSc CFL on power density are more significantly observed. So LSSc is effective for increasing power density and preventing cross-over of protons at lower temperatures.

The increase in power density with the LSSc CFL was analysed using impedance measurement, and Fig. 3 shows the EIS spectra at 973 and 773 K. The overall EIS of PCFCs shows a much smaller overvoltage with the LSSc CFL, which is almost 1/4 of that observed on the non CFL cell, suggesting that the LSSc CFL significantly enhances cathodic activity, as shown in Fig. S3.† In Fig. 3a, non CFL exhibits a large ohmic resistance of 1.16 Ω cm^2, which dominated the internal resistance of the cell. In contrast, the deposition of the LSSc CFL decreased the ohmic resistance. The estimated IR loss values for the non, LSSc10, LSSc15, LSSc20, and LSSc25 cells were 1.15, 0.39, 0.32, 0.34, and 0.44 Ω cm^2, respectively. The decrease in ohmic resistance suggests that there was significant contact resistance at the cathode/BZCY interface, which was decreased by the increased proton conductivity through the LSSc film. Contact resistance is affected by the charge transfer at the electrode/electrolyte interface, which is the reaction site in PCFCs. This interface requires high proton conductivity to facilitate proton transport, decreasing the IR resistance. Insertion of a dense LSSc CFL at the interface results in lower ohmic resistance, which suggests that proton conductivity was improved by the LSSc CFL. Decrease in ohmic resistance with the LSSc CFL was particularly observed at 773 K, as shown in Fig. 3b. This increase in proton conductivity facilitates interaction with O^{2-} at the electrode/electrolyte boundary, leading to lower IR resistance and enhanced charge transfer. For these reasons, there is a strong correlation between proton conductivity and IR resistance in PCFCs. On the other hand, more significant effects of the LSSc CFL were observed on the decreased overvoltage. At 973 K, the impedance semicircle was already small even in the cell without the LSSc CFL, indicating reasonably high electrode activity. Therefore, the insertion of the CFL does not significantly decrease the overvoltage. However, at 773 K, the semicircle in the impedance plots increased in the cell without the CFL. At least two semicircles were observed in the higher and lower frequency regions. These impedance semicircles were considerably decreased by the insertion of the LSSc CFL, particularly the semicircle at higher frequencies. The smallest semicircles were observed with the LSSc15 CFL, indicating a significant decrease in polarization resistance from 8.28 Ω cm^2 in the non CFL to 1.69 Ω cm^2 (R_p of LSSc15 CFL) at 773 K. From the impedance analysis of the internal resistance of the cell, the increase in power generation of the BZCY cell with the LSSc CFL can be explained by the decreased ohmic resistance and also overvoltage, which may be the cathodic activity for proton oxidation. In Fig. 3c, this model includes resistance (R_s), which represents the electrolyte resistance, followed by two parallel RC circuits of polarization resistances (R_{P_1} and R_{P_2}) and constant phase elements (CPE1 and CPE2). This model accurately shows the electrochemical behavior of the cell.

DRT analysis was commonly used for impedance analysis within the frequency range of 0.1 to 10^5 Hz. Fig. 4 shows the DRT analysis results of the impedance data shown in Fig. 3 at 973 K, and the temperature dependence of the LSSc15 CFL. Two distinct DRT peaks (P_1, P_2) were observed at 973 K by semicircle fitting, and so two phenomena were mainly included in the impedance arc shown in Fig. 4a. The P_2 peak observed at higher frequencies may be related to an anodic reaction step, and the P_2 peak was significantly decreased by the insertion of the LSSc CFL. This suggests that LSSc is effective in facilitating gas diffusion to the three-phase boundary (TPB) at the cathode.[27] Also, it is reported that LSSc shows large water uptakes, which means a high H^+ concentration. As a result, diffusion and reaction at the cathode seem to be accelerated by the LSSc CFL on the BZCY film. On the other hand, the P_1 peak, appearing at lower frequencies, is associated with proton oxidation at the TPB and was also decreased by the insertion of LSSc10 and LSSc15 CFL. Thus, LSSc10 or LSSc15 is highly effective for increasing SSC cathode activity, particularly in oxygen dissociation and proton oxidation.

High-density LSSc film affects proton transport and electrochemical reactions at the cathode/electrolyte interface, which is an important part of mass transport in PCFCs. With regard to mass transport in these systems, the LSSc CFL enhances the proton conductivity, thereby improving mass transport to the

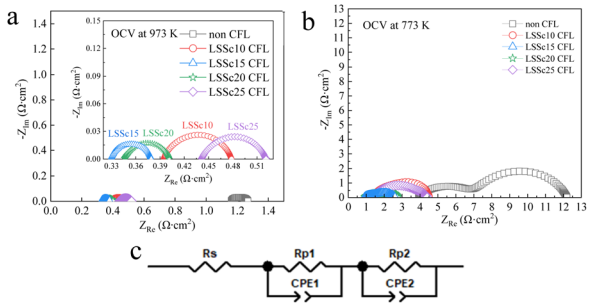

Fig. 3 EIS spectra of PCFCs with non, LSSc10, LSSc15, LSSc20 and LSSc25 CFL at (a) 973 and (b) 773 K.

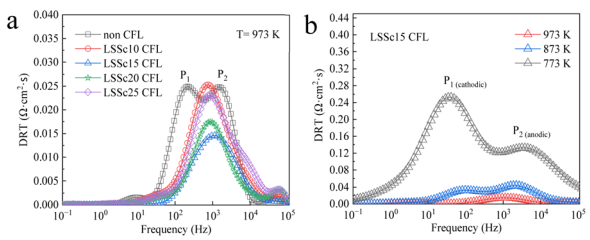

Fig. 4 DRT spectra of PCFCs with non, LSSc10, LSSc15, LSSc20, and LSSc 25 CFL at (a) 973 K and (b) temperature dependence of LSSc15.

active sites and increasing the performance. As analyzed by DRT spectra, a decrease in resistance at the interface was associated with improved proton oxidation activity. Fig. 4b shows the DRT results of the LSSc15 CFL in the temperature range from 773 to 973 K. As the temperature decreased, the electrical conductivity and gas diffusion decreased from the cathodic reaction step, resulting in an increased DRT peak at low frequencies of P_1. As a result, the resistance associated with the interface reaction at the cathode side decreased, and the peak at lower frequencies also decreased at 773 K due to the LSSc CFL.

To analyse the effect of the LSSc CFL on internal resistance under polarized conditions, IR loss and overvoltage were measured with the current interruption method as a function of current density. Fig. 5 shows the IR loss and overvoltage of the cell with and without the LSSc CFL at 973 and 773 K. As indicated by impedance analysis under open-circuit conditions, IR loss dominated the internal resistance as shown in Fig. 5a and c. In particular, at 773 K, the IR drop significantly increased, however it drastically decreased with LSSc CFL. In contrast, overvoltage is not large at 973 K and sustained a small value even at 773 K when the LSSc CFL was inserted, as shown in Fig. 5b and d. For example, the overvoltages of the cell with LSSc 15 and 20 CFL were smaller than 30 mV at 210 mA cm^{-2} and 773 K. As a result, the increased power density of the PCFCs with LSSc CFL was attributed to the decreased IR loss and overvoltage of the electrode suggesting that the LSSc interlayer is highly effective for increasing the cathodic performance of the SSC cathode.

One reason for this increased cathodic performance is the decreased proton crossover by the LSSc interlayer. Proton crossover, caused by partial hole conductivity, was analyzed by measuring the humidity on the cathode side using a dew point meter. Fig. 6 shows the estimated leakage current as a function of current density.

Leakage current is associated with partial hole conductivity in BZCY in a high pO_2 range and it decreased the performance of PCFCs.[28] As shown in Fig. 6a, the dew point increased with

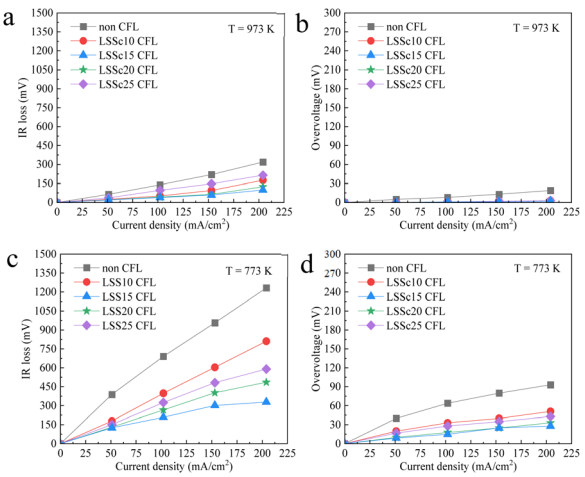

Fig. 5 Internal resistance of PCFCs with non, LSSc10, LSSc20 and LSSc 25 CFL at (a and b) 973 K and (c and d) 773 K.

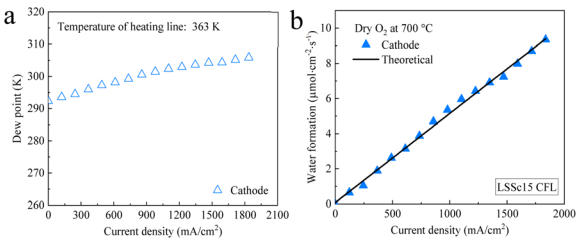

Fig. 6 (a) Dew point as a function of current density and (b) estimated water formation in LSSc15 CFL under dry O_2 conditions at 973 K.

current density, indicating that water was formed at the cathode side by the oxidation of protons. Under OCV conditions, there is no humidity formed and this is in stark contrast with BZCY without LSSc CFL.[29] In the case of BZCY, high humidity was observed under OCV conditions suggesting the crossover of protons by partial hole conduction. As shown in Fig. 6b, water formation was estimated from the dew point (t) and the estimated humidity is also shown in Fig. 6b from Faraday's law as a dashed line. It is seen that the observed amount of humidity well fits with the theoretical line. With the OCV close to the theoretical value, the LSSc15 interlayer effectively prevented H^+ crossover. Preventing the crossover of proton is highly important for increased efficiency of PCFC and so LSSc CFL is also useful from an efficiency point of view.

In Fig. 7, the cross-sections of the BZCY film and Ni–Fe porous substrate are observed with SEM after PCFC measurements. Fig. 7a shows the surface of the deposited LSSc film, which was dense and had uniform morphology without any formation of pinholes or cracks. Fig. 7b and c show the Ni–Fe bimetallic substrate with a porous cross-section, and also a dense, crack-free BZCY film with a thickness of 10 μm. This SEM image confirms the successful preparation of metal supported PCFCs by the PLD method. Furthermore, Fig. 7d shows SEM observation results of the LSSc film, demonstrating that the 200 nm thick, dense LSSc CFL was successfully deposited and remained after power generation measurements. A uniform and dense BZCY film with 10 μm thickness was also observed. Ni diffusion into the BZCY film is another issue due to the formation of highly resistive secondary phases, which could result in decreased power density. However, Ni diffusion was hardly observed in the electrolyte, cathode, or anode, as

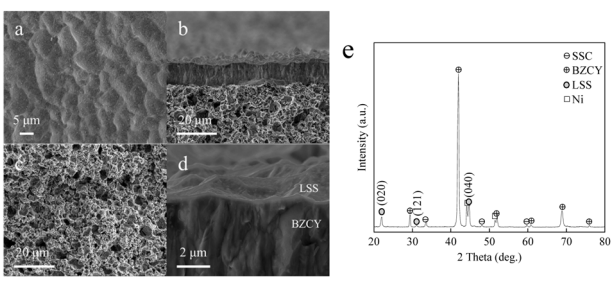

Fig. 7 (a) SEM image of the surface, (b) cross-section of the BZCY film, (c) cross-section of the Ni–Fe substrate, (d) enlarged LSSc CFL, and (e) XRD pattern of PCFCs with LSSc15 CFL after the cell test.

confirmed by EDS line analysis with EDS mapping as shown in Fig. S4.† To further confirm the prevention of undesired Ni diffusion, XRD analysis of the PCFCs with the CFL was performed as shown in Fig. 7e. The diffraction peaks were assigned to the SSC cathode, BZCY electrolyte, LSSc CFL, and the Ni from the reduced anode. XRD patterns from BZCY and LSSc films suggested the distinct orientations as indicated by strong diffraction peaks from LSSc (040) and BZCY (024). The effects of LSSc film thickness were further studied from the power generation performance as shown in Fig. 8.

PCFCs with 200 nm thick LSSc CFL deposited on a BZCY electrolyte showed excellent electrochemical performance as discussed. However, compared to the 200 nm thick CFL, the power density decreased to 500 mW cm^{-2} on the cell with a thicker LSSc film (500 nm), as shown in Fig. 8a. Fig. 8b shows the EIS spectra of the cell with CFL layers of different thicknesses (200 and 500 nm) at a temperature of 973 K. The ohmic resistance of the cell with 500 nm LSSc was 0.55 Ω cm^2 which was much larger than that of 200 nm (0.34 Ω cm^2). In addition, overvoltage also increased from 0.055 to 0.1 Ω cm^2 on moving from 200 to 500 nm CFL. The decreased power density of the cell using thicker LSSc CFL was assigned to such increased IR loss and overvoltage because of the lower electrical conductivity of LSSc. Increased overvoltage was also confirmed under polarized conditions as shown in Fig. 8c. On the other hand, it is considered that a too thin CFL is also not desirable because of the small effect on proton concentration at the interface as discussed later. Considering the superior power generation properties as shown in Fig. 8, the optimal thickness of the LSSc CFL seems to be around 200 nm.

Fig. 9 shows the XPS spectra of La, Sr, Sc, and O in LSSc bulk and 200 nm film on the Al_2O_3 substrate. Compared with bulk LSSc, the binding energies of La and Sr hardly changed, indicating almost no change in the oxidation states of La^{3+} and Sr^{2+} (Fig. 9a and b). In contrast, the binding energy of Sc 2p in the LSSc film was shifted to a larger value compared to that in bulk, suggesting a slightly oxidized state of Sc in the CFL (Fig. 9c). This implies that electron holes may be localized at Sr^{3+} in the

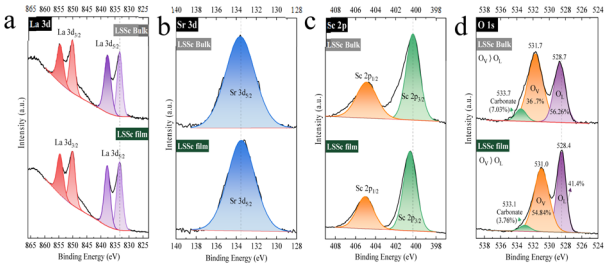

Fig. 9 XPS spectra of La 3d, Sr 3d, Sc 2p, and O 1s in LSSc bulk and LSSc film.

nano-thick film, resulting in decreased hole concentration by trapping. The O 1s spectra of Fig. 9d consist of three peaks, which were assigned to oxygen vacancies (O_V), lattice oxygen (O_L), and surface adsorption species like carbonate at 528.4, 531, and 533.1 eV, respectively, on LSSc. Compared to the bulk, the film shows a higher concentration of oxygen vacancies, which could lead to an increase in proton concentration. According to the Grotthuss mechanism,[30] proton formation occurs *via* the interaction of water with oxygen vacancy sites as shown in eqn (1):

$$V_O^{\cdot\cdot} + H_2O = O_O^{\times} + H_i^{\cdot} \quad (1)$$

So the increased peak area at 528.4 eV in the LSSc film suggests a higher interstitial proton concentration in nano-thick films. This may be related to the increased lattice strain from the mismatch between LSSc and BZCY lattice size.

The change in proton conductivity in the LSSc film was further measured with electrochemical conductivity.

Fig. 10a shows the electrical conductivity of the film and bulk LSSc samples under humid H_2 conditions. Both samples exhibit high conductivity. However, the LSSc film shows a conductivity of $\log \sigma$ (S cm^{-1}) = −1.98, which is higher than that of the bulk conductivity of −2.16 S cm^{-1} at 973 K. As observed in XPS O 1s spectra, the LSSc film contains a significantly higher concentration of protons owing to the increased amount of oxygen vacancies (36.7%). This suggests that higher proton conductivity was achieved in the film than in bulk LSSc. As the temperature decreases, conductivity also decreases, and the LSSc film shows a low activation energy of 0.16 eV, indicating increased proton conductivity in the LSSc film at low temperature. Therefore, increased conductivity may be attributed to the

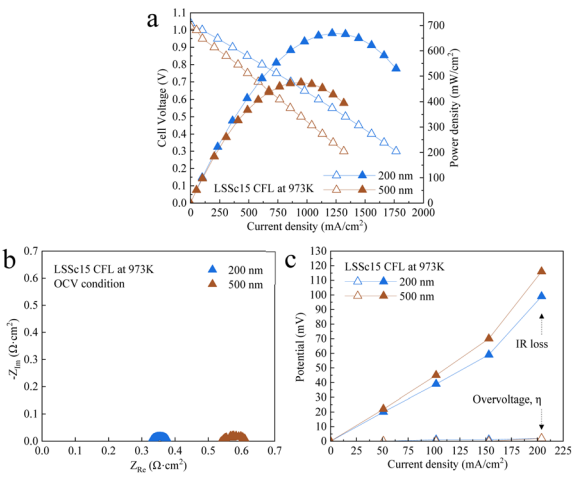

Fig. 8 Effects of LSSc film thickness on PCFC performance: (a) *I*–*V*, *I*–*P* curves, (b) EIS spectra, (c) cathodic overvoltage.

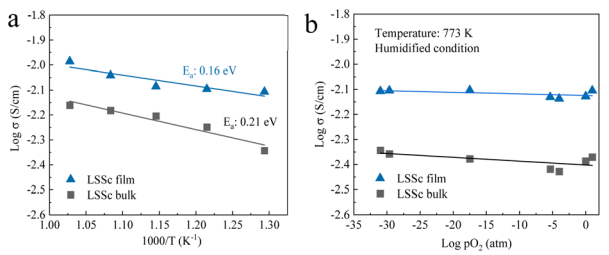

Fig. 10 Comparison of (a) electrical conductivity in H_2 and (b) pO_2 dependence of LSSc film and bulk at 573 K.

increased proton concentration owing to the formation of larger amount of oxygen vacancies as shown in Fig. 9. Fig. 10b shows pO_2 dependence of conductivity and the conductivity of bulk LSSc decreased as pO_2 decreased in a high pO_2 range higher than 10^{-5} atm, suggesting that hole conductivity was dominant in the high pO_2 range in the case of bulk LSSc as reported by Nomura *et al.*[12] In contrast, the conductivity of LSSc film was almost independent of pO_2, indicating that hole conductivity was significantly suppressed in the LSSc film. Considering the partially oxidized state of Sc suggested by XPS, holes seem to be trapped at Sc sites resulting in the decreased conductivity. This observation also well corresponded with the increased OCV and almost no crossover of proton in the BZCY cell with the LSSc CFL.

Since hole conductivity was suppressed in the LSSc film, changes in hole concentration and mobility were further estimated by using Hall effect measurements. These measurements were performed to investigate the hole conductivity in the LSSc film and bulk under humidified H_2 conditions at temperatures from 773 to 973 K. Positive Hall coefficients (V_{Hall}) were observed on both samples and electron holes are the main electronic charge carriers in the film and bulk, consistent with hole formation as described by the following equation (eqn (2)):

$$1/2O_2 + V_O^{\cdot\cdot} = O_O^{\times} + 2h^{\cdot} \quad (2)$$

From the Hall coefficient and resistance, hole concentration and its mobility were estimated. Fig. 11a shows the hole mobility in the film and bulk under 3% H_2O–H_2 conditions. LSSc film exhibits higher hole mobility (1160 $cm^2\ N^{-1}\ s$) at 973 K, which corresponds to its higher electrical conductivity and is associated with a higher oxygen vacancy concentration, as suggested by XPS analysis compared to bulk LSSc. In contrast, as shown in the ESI (Fig. S5a and b†), BZCY film shows low hole mobility and high hole concentration.

Fig. 11b shows the estimated hole concentration in LSSc bulk and film, suggesting that the LSSc film maintains a much lower hole concentration under the measurement conditions. This is attributed to holes being trapped on Sc site in the LSSc film, as suggested by XPS analysis. Fig. 11c compares the electrical conductivity of LSSc film and bulk. Due to the contact resistance between the sample and the probe, the measured conductivity was slightly lower than that shown in Fig. 10. Under humidified H_2 conditions, LSSc film demonstrates higher conductivity at 973 K compared to LSSc bulk and BZCY film, which is the crucial role of hole concentration in determining overall electrical conductivity, as shown in Fig. S5c.†

To evaluate the concentration of protons, the temperature dependence of weight change between 298 and 973 K under a dry N_2 atmosphere was measured using thermogravimetry (TG) after exposure to humidified N_2, as shown in Fig. 12. The larger weight loss observed in LSSc film than in bulk suggests a higher concentration of oxygen vacancies[31,32] under dry N_2 compared to the BZCY film and LSSc bulk as shown in Fig. 12a. This weight loss is attributed to the desorption of physically adsorbed water and/or chemically bounded hydroxyl groups. Fig. 12b shows the hydration properties of BZCY, LSSc film and LSSc bulk. Before measurement, all samples were heated up to 700 °C in a dry N_2 atmosphere to remove surface water molecules. To assess hydration properties, TG curves of samples were obtained under 3 vol% H_2O–N_2 (humidified N_2) during the cooling process. To prevent rapid evaporation, the temperature is slowly decreased. BZCY film exhibits a small weight increase (0.047), indicating limited hydration capacity compared to LSSc, including film and bulk.[32–34] This implies that LSSc has more efficient binding sites for hydration capacity compared to BZCY. The high concentration of protons in the LSSc film was also confirmed by FT-IR spectra as shown in Fig. S6 in the ESI.† The presence of water vapor facilitates the incorporation of hydroxyl groups, as shown in eqn (1), which enhances proton conduction. The high hydration capacity of LSSc suggests increases in proton conductivity due to larger amount of oxygen vacancies.

As discussed, the LSSc15 CFL achieves a significantly increased power density of 233 mW cm^{-2} at 773 K. This enhancement in power density may be attributed to the increased proton conductivity at the cathode interface.

The effects of humidity in O_2 on the power density are shown in Fig. 13 at 973 K. In this experiment, oxygen with 3% humidity was used as the oxidant. Although the OCV was nearly identical between the cell with and without humidity in O_2, the maximum power density increased with humidity as shown in Fig. 13a. The impedance analysis results are shown in Fig. 13b, comparing the cell under dry and humidified O_2. Although IR

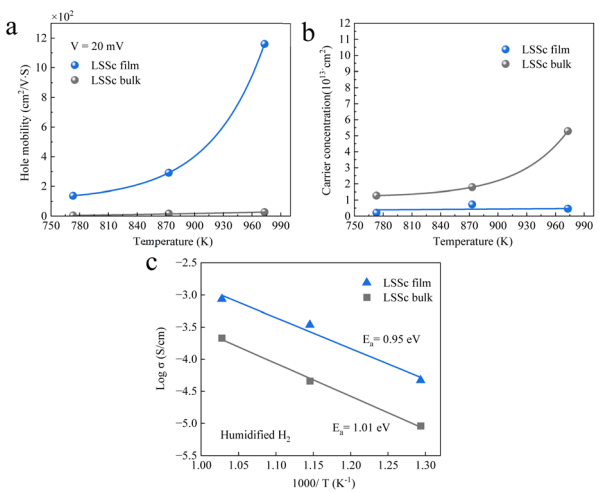

Fig. 11 (a) Hole mobility, (b) carrier concentration, (c) conductivity of LSSc film and bulk under humidified (3% H_2O) H_2 conditions.

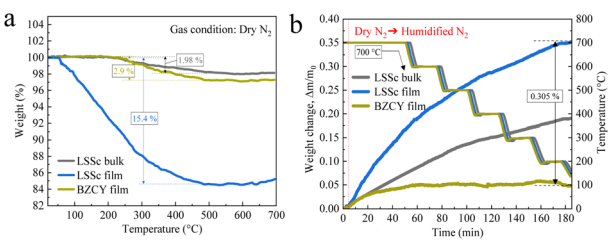

Fig. 12 (a) Weight loss (dry N_2) and hydration (humidified N_2) in the TG curve of BZCY and LSSc film.

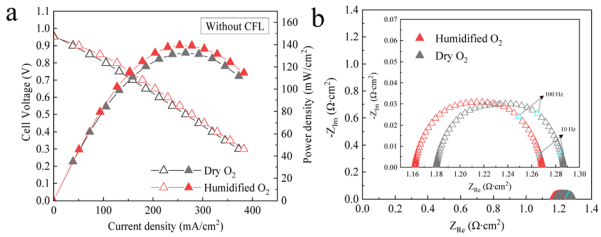

Fig. 13 Effects of H_2O in O_2 for the cathode side on power generation properties and cathodic overvoltage at 973 K (a) *I–V*, *I–P* curve, (b) EIS.

loss is almost independent of humidity in O_2, as shown in the ESI (Fig. S7†), the impedance semicircle in the lower frequency region, which may be assigned to the cathodic overvoltage, decreased with increasing P_{H_2O} in O_2. Therefore, the increased power density can be attributed to enhanced proton conductivity at the cathode/electrolyte interface. The increased proton conductivity at the cathodic interface is effective in decreasing cathodic overvoltage.

At the cathode, the following reaction occurs.

$$1/2O_2 + V_O^{\cdot\cdot} + 2e^- = O_O^{\times} \quad (3)$$

$$O_O^{\times} + 2H_i^{\cdot} = H_2O + V_O^{\cdot\cdot} \quad (4)$$

The mechanism of the increased performance of PCFCs by LSSc CFL is schematically shown in Fig. 14. Compared to BZCY, LSSc originally has a high proton concentration, as suggested by the larger amount of adsorbed water. In addition, in the nano-thickness film, the proton concentration in LSSc may be further enhanced due to further increase in hydration amount (Fig. 12b), change in chemical equilibrium from oxygen absorption (hole) to water (proton), and the suppression of hole conductivity by trapping at the Sc site. This means that the hole formation by eqn (2) is suppressed in the LSSc film, while the number of protons through the uptake of H_2O, as expressed in eqn (1), was increased by the tensile strain formed (volume of the unit lattice of LSSc and BZCY is 266.652 Å^3 and 489.144 Å^3, respectively). Since the cathodic overvoltage decreases with increasing water partial pressure in O_2, the increased proton concentration at the SSC/LSSc cathodic interface is highly effective in decreasing the cathodic overvoltage. This suggests that the increase in proton concentration in eqn (4) can shift to the right side, resulting in the increased cathodic activity and so decreased cathodic overvoltage.

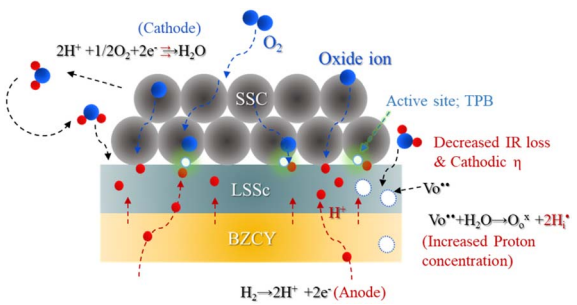

Fig. 14 Schematic image of the positive effects of LSSc CFL on the cathodic reaction of PCFCs.

As shown in Fig. 14, water formed on the cathode side is also expected to result in increased proton concentration at the cathodic interface. Furthermore, the increased proton conductivity in the LSSc film also decreases IR loss and also proton crossover (leading to an increase in OCV) at the cathode interface. These positive effects of the LSSc film are more significantly observed at 773 K because the water uptake and consequently proton concentration in the LSSc film increases as the temperature decreases. This study reveals that the LSSc CFL is highly effective in increasing the power density as well as OCV of metal-supported PCFC with the BZCY electrolyte, even though such significant positive effects of LSSc have not been previously reported.

3. Conclusions

Effects of an LSSc film as a cathodic functional layer on the power generation properties of PCFC using BZCY electrolyte on a Ni–Fe porous metal anode support were studied. It was found that 200 nm LSSc CFL was highly effective for increasing the power density of PCFCs using 10 μm thick BZCY film, in particular, at low temperature. The open circuit voltages were 1.04 V and 1.15 V, and maximum power densities were 668 and 233 mW cm^{-2} achieved at 973 and 773 K, respectively. Fig. S8† shows the temperature dependence of the power generation properties of PCFCs, with the LSSc 15 CFL showing higher performance compared to conventional reported cells (Tables S3 and S4†), particularly at 773 K. Our cell with LSSc 15 CFL demonstrates one of the highest power densities in PCFCs with the BZCY electrolyte. Furthermore, the OCV of PCFC using BZCY film is typically smaller than the theoretical value which means decreased efficiency. The almost theoretical OCV at 773 K achieved by LSSc CFL is highly important for the high conversion efficiency of PCFC, which is most strongly required. The improved performance of the PCFCs is attributed to the decreased cathodic overvoltage and ohmic loss, which is explained by the high proton concentration in the LSSc interlayer between the BZCY electrolyte and SSC cathode. Additionally, in the nano-thick film, the proton concentration was much higher. The insertion of the LSSc CFL enhanced the proton concentration at the three-phase boundary of the SSC cathode, leading to a significant decrease in cathodic overvoltage. This increased proton concentration in the LSSc film is the origin of the improved performance of the metal supported BZCY cell. Consequently, 15% Sr-doped $LaScO_3$ with 200 nm is highly promising as a cathode functional layer for PCFCs. Durability is another important subject. We expect that the LSSc interlayer may have positive effects on long term stability by enhancing the interface reaction and low mechanical degradation between layers. This is due to the perovskite structure of LSSc, its high proton conductivity, and low reactivity with the electrolyte. This aspect will be studied in future.

4. Experimental

4.1 Cell preparation

A porous Ni–Fe metal pellet was prepared as the anode support for the PCFCs using the selective reduction of a dense disc

consisting of NiO–$NiFe_2O_4$ composites, which was prepared by the impregnation method. The molar ratio of Ni to Fe in the solution was set at 9 : 1. To prepare the composite powder, $Fe(NO_3)_3 \cdot 9H_2O$ (99%, Wako Co.) and NiO (99%, Wako Co.) were used as starting materials, mixed in 200 mL of distilled water at a concentration of 10 wt% Fe_2O_3, and continuously stirred to facilitate evaporation. After gelation, calcination was performed at 873 K for 4 h to decompose the nitrate. The resulting mixed powder was subjected to a second calcination at 1473 K in air for 6 h to enhance crystallinity. To achieve a uniform and fine particle size, the mixed powder was treated in a ball mill with zirconia balls (Ø: 10 mm) for 5 h in ethanol. Subsequently, the dried powder was pressed into pellets (20 mm in diameter) at 30 MPa using a uni-axial press, followed by cold isostatic pressing (CIP) at 270 MPa for 30 min. The resulting pellets were pre-calcined at 1273 K for 6 h, polished, and then sintered at 1723 K for 6 h. A highly dense NiO–$NiFe_2O_4$ pellet was used as the substrate for the PCFC with a BZCY film. Fig. S9† shows the fabrication procedure of the anode metal-supported PCFCs (LSSc/BZCY/Ni–Fe) used in this study. The fabrication began with the preparation of a dense precursor of NiO–$NiFe_2O_4$ as the substrate. On the substrate, BZCY and LSSc layers were deposited *via* PLD techniques at 1073 K. Following the deposition step, the cathode material was screen printed onto the cell. The H_2 reduction process was then conducted, during which NiO was initially reduced to metallic Ni, preventing large shrinkage of the anode substrate. Subsequently, the reduction of iron oxide proceeded, resulting in the formation of a Ni–Fe bimetallic support and porous Ni–Fe metal supported PCFCs with LSSc CFL. Further details of each layer are explained as below and also in our previous report.[35]

$BaZr_{0.44}Ce_{0.36}Y_{0.2}O_3$ (BZCY) was used as the electrolyte for the PCFC, and the BZCY film was prepared using the pulsed laser deposition (PLD) method. BZCY powder with the stoichiometric ratio was prepared using the Pechini process, involving citric acid and a nitrate solution. The calculated metal nitrates were dissolved in 200 mL of distilled water and then evaporated to dryness, followed by calcination at 1723 K for 6 h. LSSc powder was prepared using the solid-state reaction method. The calculated amount of starting oxide powder was mixed using a ball mill (Mixer Mill MM500 nano, Retsch) with zirconia balls (Ø: 3 mm) for 1.5 h in an ethanol solution, followed by calcination at 1723 K for 6 h. The prepared BZCY and LSSc powders were pressed into pellets (20 mm in diameter) at 270 MPa using CIP for 30 minutes and sintered at 1723 K for 6 h.

BZCY and LSSc films were deposited on the dense NiO–$NiFe_2O_4$ composite substrate or ZrO_2 plate (Japan Fine Ceramic Co. Ltd) using PLD (PLD-7, PASCAL, Japan) with a KrF excimer laser operating at a wavelength of 248 nm, 180 mJ per pulse, and a frequency of 10 Hz at 1073 K under an oxygen partial pressure of 1.0 Pa for BZCY and 0.67 Pa for LSSc, respectively. The target and substrate were rotated to ensure uniform film deposition. Subsequently, the deposited films were calcined at 1073 K, consistent with the deposition conditions.

$Sm_{0.5}Sr_{0.5}CoO_3$ (SSC), prepared using the solid-state reaction method, was used for the cathode. The SSC slurry was prepared by mixing ethyl cellulose (0.06 g) with a small amount of 3-hydroxyl-2,2,4-trimethylpentyl isobutyrate, which was then coated onto the LSSc/BZCY film using a screen-printing method (Ø: 5 mm), followed by calcination at 1073 K for 1 h. The NiO–$NiFe_2O_4$ was reduced at 973 K in a H_2 flow, resulting in the preparation of the metal supported single cell, Ni–Fe/BZCY/LSSc/SSC.

4.2 Characterization

The power generation performance of the PCFCs was measured using a four-probe method, applying a constant current with a galvanostat (Hokuto Denko, HA-301) and measuring the potential with a digital multimeter (Advantest R6451A). Humidified O_2 and H_2 were supplied to the cathode and anode sides, respectively, using a water bubbler, at a total flow rate of 100 mL min^{-1}. The internal resistance was estimated using the current interruption method and electrochemical impedance measurements, employing an impedance/gain-phase analyzer (Solartron type 1260) in conjunction with an electrochemical interface (Solartron type 1270) under open circuit voltage (OCV) conditions. Morphological characterization was conducted using scanning electron microscopy (SEM, VE-7800, KEYENCE, Japan) and energy dispersive X-ray spectrometry (EDS). X-ray diffraction (XRD) measurements were performed with a commercial diffractometer (XRD, RINT-2500, Rigaku, Japan) with a CuKα line. X-ray fluorescence (XRF-1800, SHIMADZU, Japan) was used to analyse the composition of the bulk and films. The oxidation states of elements in the films were investigated using X-ray photoelectron spectroscopy (XPS, Kratos Ultra2, SHIMADZU Corp., Japan). Carbon peaks were used as the internal standard. The Hall effect was measured using a Lake Shore 8400 Hall measurement system. FT-IR was measured with a commercial spectrometer (610, JASCO Co.) with an MCT detector. TG measurement was performed with TG-DSC equipment (STA Jupiter, NETZSCH) in a N_2 atmosphere. The samples were heated to 973 K under dry conditions for dehydration. Consequently, 3% humidified N_2 was made to flow for water uptake at 973 K. The TG continuously measured weight changes as the sample absorbed water, showing hydration. The weight gain was observed to determine the hydration capacity of the proton conductor with decreasing temperature from 973 to 298 K. The LSSc film on an Al_2O_3 substrate (29.6 mg, 3 × 3 mm) and LSSc powder (29.0 mg) were used for measurement.

Data availability

The data supporting this article are openly available and have been included as part of the ESI.†

Author contributions

Hyo-Young Kim: writing-original draft, writing-review and editing, conceptualization, data curation, investigation, visualization; Motonori Watanabe, Jun Tae Song, Miki Inada: investigation; Tatsumi Ishihara: conceptualization, funding acquisition, supervision, writing-review & editing.

Conflicts of interest

There are no conflicts to declare.

Acknowledgements

This study was supported by the New Energy and Industrial Technology Development Organization (NEDO) of Japan under project number JPNP20003.

References

1 B. Stambouli and E. Traversa, *Renewable Sustainable Energy Rev.*, 2002, **6**, 433–455.
2 H. Choudhury, A. Chandra and A. Arora, *Renewable Sustainable Energy Rev.*, 2013, **20**, 430–442.
3 N. Q. Minh, *Solid State Ionics*, 2004, **174**, 271–277.
4 L. Fan, B. Zhu, P. C. Su and C. He, *Nano Energy*, 2018, **45**, 148–176.
5 Z. Shao and S. M. Haile, *Nature*, 2004, **431**, 170–173.
6 K. D. Kreuer, *Annu. Rev. Mater. Res.*, 2003, **33**, 333–359.
7 C. Duan, J. Huang, N. Sullivan and R. O'Hayre, *Appl. Phys. Rev.*, 2020, **7**, 011312.
8 D. Zou, Y. Yi, Y. Song, D. Guan, M. Xu, R. Ran, W. Wang, W. Zhou and Z. Shao, *J. Mater. Chem. A*, 2022, **10**, 5381–5390.
9 X. Wang, W. Li, C. Zhou, M. Xu, Z. Hu, C. W. Pao and Z. Shao, *ACS Appl. Mater. Interfaces*, 2022, **15**, 1339–1347.
10 K. Akimoto, N. Wang, C. Tang, K. Shuto, S. Jeong, S. Kitano and Y. Aoki, *ACS Appl. Energy Mater.*, 2022, **5**, 12227–12238.
11 M. Wang, C. Su, Z. Zhu, H. Wang and L. Ge, *Composites, Part B*, 2022, **238**, 109881.
12 L. Malavasi, C. A. J. Fisher and M. S. Islam, *Chem. Soc. Rev.*, 2010, **39**, 4370–4387.
13 K. Nomura, T. Takeuchi, S. I. Kamo, H. Kageyama and Y. Miyazaki, *Solid State Ionics*, 2004, **175**, 553–555.
14 Y. Stroeva and V. P. Gorelov, *Russ. J. Electrochem.*, 2012, **48**, 1079–1085.
15 H. Kato, T. Kudo, H. Naito and H. Yugami, *Solid State Ionics*, 2003, **159**, 217–222.
16 H. Hayashi, H. Inaba, M. Matsuyama, N. G. Lan, M. Dokiya and H. Tagawa, *Solid State Ionics*, 1999, **122**, 1–15.
17 V. Kuzmin, A. Y. Stroeva, M. S. Plekhanov, V. P. Gorelov and A. S. Farlenkov, *Int. J. Hydrogen Energy*, 2018, **43**, 19206–19212.
18 S. Farlenkov, M. I. Vlasov, N. M. Porotnikova, I. A. Bobrikov, A. V. Khodimchuk and M. V. Ananyev, *Int. J. Hydrogen Energy*, 2020, **45**, 23455–23468.
19 N. Tsvetkov, D. Kim, I. Jeong, J. H. Kim, S. Ahn, K. T. Lee and W. Jung, *Adv. Mater. Technol.*, 2023, **8**, 2201075.
20 D. Pergolesi, E. Fabbri, A. D'Epifanio, E. Di Bartolomeo, A. Tebano, S. Sanna and E. Traversa, *Nat. Mater.*, 2010, **9**, 846–852.
21 Y. Liu, H. Li, C. Cai, S. Li, J. Cui and S. An, *ACS Omega*, 2023, **8**, 8011–8018.
22 K. Bae, H. S. Noh, D. Y. Jang, J. Hong, H. Kim, K. J. Yoon and J. W. Son, *J. Mater. Chem. A*, 2016, **4**, 6395–6403.
23 T. Ishihara, M. Honda, H. Nishiguchi and Y. Takita, *ECS Proceedings*, 1997, **1997**(1), 301.
24 N. Sivakumar, J. Gajendiran, A. Alsalme and K. Tashiro, *Physica B*, 2022, **641**, 414086.
25 A. S. Lesnichyova, S. A. Belyakov, A. Y Stroeva and A. V. Kuzmin, *Ceram. Int.*, 2021, **47**, 6105–6113.
26 R. D. Shannon, *Acta Cryst.*, 1976, **32**, 751–767.
27 H. Sumi, H. Shimada, Y. Yamaguchi, Y. Mizutani, Y. Okuyama and K. Amezawa, *Sci. Rep.*, 2021, **11**, 10622.
28 L. Malavasi, C. A. J. Fisher and M. S. Islam, *Chem. Soc. Rev.*, 2010, **39**(11), 4370–4387.
29 K. D. Kreuer, *Annu. Rev. Mater. Res.*, 2003, **33**, 333–359.
30 Y. Wang, Y. Ling, B. Wang, G. Zhai, G. Yang, Z. Shao and T. Li, *Energy Environ. Sci.*, 2023, **16**, 5721–5770.
31 T. Miruszewski, K. Dzierzgowski, P. Winiarz, S. Wachowski, A. Mielewczyk-Gryń and M. Gazda, *Materials*, 2020, **13**, 965.
32 C. Lu, R. Ren, Z. Zhu, G. Pan, G. Wang, C. Xu and K. Sun, *Chem. Eng. J.*, 2023, **472**, 144878.
33 J. Hyodo, K. Tsujikawa, M. Shiga, Y. Okuyama and Y. Yamazaki, *ACS Energy Lett.*, 2021, **6**, 2985–2992.
34 S. Pirou, Q. Wang, P. Khajavi, X. Georgolamprou, S. Ricote, M. Chen and R. Kiebach, *Int. J. Hydrogen Energy*, 2022, **47**, 6745–6754.
35 H. Y. Kim, M. Watanabe, J. T. Song, M. Inada and T. Ishihara, *ACS Appl. Energy Mater.*, 2024, **7**, 7945–7955.

